

# High-Curie-temperature ferromagnetism in self-organized $\text{Ge}_{1-x}\text{Mn}_x$ nanocolumns

MATTHIEU JAMET<sup>1\*</sup>, ANDRÉ BARSKI<sup>1</sup>, THIBAUT DEVILLERS<sup>1</sup>, VALIER POYDENOT<sup>1</sup>, ROMAIN DUJARDIN<sup>1</sup>, PASCALE BAYLE-GUILLEMAUD<sup>1</sup>, JOHAN ROTHMAN<sup>2</sup>, EDITH BELLET-AMALRIC<sup>1</sup>, ALAIN MARTY<sup>1</sup>, JOËL CIBERT<sup>3</sup>, RICHARD MATTANA<sup>1†</sup> AND SERGE TATARENKO<sup>4</sup>

<sup>1</sup>Département de Recherche Fondamentale sur la Matière Condensée, Service de Physique des Matériaux et Microstructures, CEA Grenoble, 17 avenue des Martyrs, 38054 Grenoble Cedex 9, France

<sup>2</sup>Laboratoire d'Electronique de Technologie de l'Information, Laboratoire Infrarouge, CEA Grenoble, 17 avenue des Martyrs, 38054 Grenoble Cedex 9, France

<sup>3</sup>Laboratoire Louis Néel, CNRS, BP166, 38042 Grenoble Cedex 9, France

<sup>4</sup>Laboratoire de Spectrométrie Physique, BP 87, 38402 Saint-Martin d'Hères, France

<sup>†</sup>Present address: Unité Mixte de Physique CNRS-Thalès, 91767 Palaiseau Cedex and Université Paris-Sud, 91405 Orsay, France

\*e-mail: matthieu.jamet@cea.fr

Published online: 9 July 2006; doi:10.1038/nmat1686

The emerging field of spintronics would be dramatically boosted if room-temperature ferromagnetism could be added to semiconductor nanostructures that are compatible with silicon technology. Here, we report a high- $T_C$  ( $>400$  K) ferromagnetic phase of (Ge,Mn) epitaxial layer. The manganese content is 6%, and careful structural and chemical analyses show that the Mn distribution is strongly inhomogeneous: we observe eutectoid growth of well-defined Mn-rich nanocolumns surrounded by a Mn-poor matrix. The average diameter of these nanocolumns is 3 nm and their spacing is 10 nm. Their composition is close to  $\text{Ge}_2\text{Mn}$ , which corresponds to an unknown germanium-rich phase, and they have a uniaxially elongated diamond structure. Their Curie temperature is higher than 400 K. Magnetotransport reveals a pronounced anomalous Hall effect up to room temperature. A giant positive magnetoresistance is measured from 7,000% at 30 K to 200% at 300 K and 9 T, with no evidence of saturation.

In spintronics applications, magnetic properties (remanent states and spin-polarized carriers) may be conveyed by conventional metallic ferromagnets or by so-called ferromagnetic semiconductors (FMS). In addition, because ferromagnetism is driven by carriers in FMS, magnetic properties may be controlled by an electrical field through the application of a gate voltage<sup>1</sup>. Among many possible applications, carrier-controlled ferromagnetism, spin injection into nanostructures and spin collection could permit giant magnetoresistance-type memories, field sensors, spin transistors and reconfigurable logics, or even quantum information processing<sup>2</sup>. Until now, semiconductor spintronics has mainly been devised based on diluted magnetic semiconductors (DMS), in which magnetic atoms randomly substitute the semiconductor atoms<sup>3,4</sup>. DMSs containing secondary phases (metallic inclusions, semiconducting ferromagnetic phase or simply concentration modulation) have seldom been studied and have usually not been well controlled. The presence of secondary phases or inhomogeneities could increase the critical temperature<sup>5</sup>, or enhance the magnetoresistance (MR) by multiplying the number of interfaces for spin scattering. Self-organization of the secondary phase could lead to arrays of interacting magnetic memory dots, or act as nanochannels for spin injection and collection in semiconductors. In this paper, we focus on (Ge,Mn) epitaxial layers with 6% Mn, which have a well-defined pattern of Mn-rich nanocolumns, and offer very attractive magnetic and magnetotransport properties up to above room temperature.

Since the discovery of a ferromagnetic order in  $\text{In}_{1-x}\text{Mn}_x\text{As}$  in 1992 (ref. 6), many other ferromagnetic DMSs have been discovered, mostly III–V and II–V types<sup>7,8</sup>. Recently, Curie temperatures ( $T_C$ ) up to 173 K have been achieved in  $\text{Ga}_{1-x}\text{Mn}_x\text{As}$ , and intense efforts have been made to reach  $T_C$  higher than room

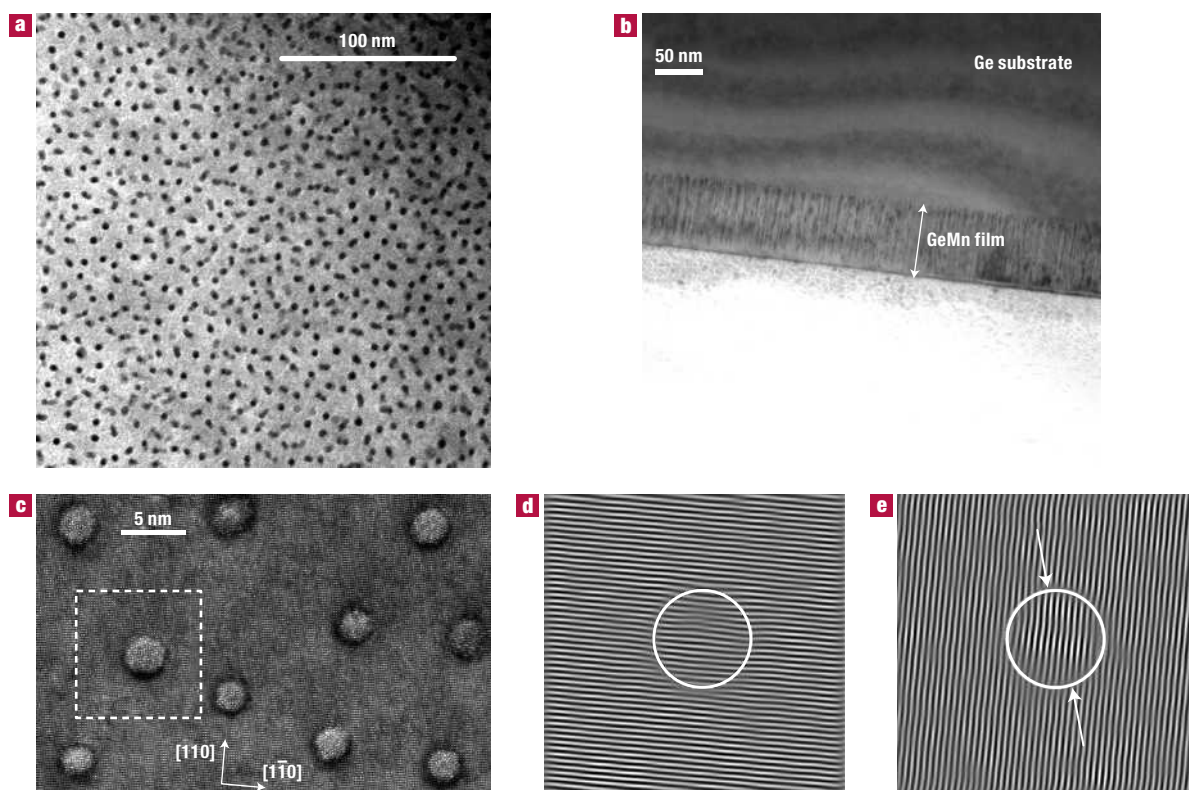


**Figure 1** Transmission electron micrographs of an 80-nm-thick  $\text{Ge}_{0.94}\text{Mn}_{0.06}$  film. **a**, Low-magnification plane view, the dark spots are nanocolumns. **b**, Low-magnification cross-sectional image of the 80-nm-thick (Ge, Mn) layer, the nanocolumns are perpendicular to the film plane and appear as dark lines. **c**, High-resolution plane view along [001] in the thinnest part of the sample. **d,e**, Bragg filtering of (220) (**d**) and (2 $\bar{2}$ 0) (**e**) diffraction spots. The dashed square in **c** shows the selected area. The nanocolumn is surrounded by a white circle and the white arrows indicate the position of dislocations.

temperature<sup>9</sup>. Surprisingly, compared with the large amount of papers dealing with III–V and II–V FMS, few works have been published on ferromagnetism in group IV semiconductors (Si, Ge, SiGe). The evidence of a ferromagnetic order in an epitaxial layer of Mn-doped germanium was first reported in 2002 by Park *et al.*<sup>10</sup>, with  $T_C$  increasing linearly with the Mn content up to 116 K for  $x = 0.035$  and a p-type doping of  $10^{20} \text{ cm}^{-3}$ . Following this initial report, some groups observed quite high ordering temperatures in (Ge, Mn) films<sup>11–15</sup>, most often without any nanoscale chemical analysis to check the homogeneity of Mn incorporation. Exceptions are ref. 10, reporting small Mn-rich precipitates, 2–6 nm in diameter, ref. 16 describing long, micrometre-sized Mn-rich stripes, and ref. 17 showing elongated Mn-rich amorphous precipitates. Zero field cooled-field cooled (ZFC-FC) or a.c. susceptibility measurements can indirectly show the presence of magnetic nanoclusters<sup>18</sup>, which could not be observed with conventional high-resolution transmission electron microscopy or X-ray diffraction (XRD) because they are too small or because their crystal axes are misoriented with respect to those of the matrix. When large enough, clusters have been reported by two groups<sup>19–22</sup>. Concerning (Ge, Mn), the most stable bulk alloys are ferromagnetic metals:  $\text{Ge}_8\text{Mn}_{11}$  ( $T_C \sim 270 \text{ K}$ ) and  $\text{Ge}_3\text{Mn}_5$  ( $T_C \sim 296 \text{ K}$ )<sup>23</sup>. However, under high growth pressures (typically a few GPa), many other bulk alloys can be synthesized which exhibit various magnetic behaviours: ferrimagnetism, ferromagnetism and antiferromagnetism. Wachtel *et al.* even showed that highly Mn-doped germanium alloys with  $x \geq 0.7$  could be ferromagnetic up to 600 K (ref. 24).

(Ge, Mn) layers were grown by molecular beam epitaxy on Ge(001) substrates. Their morphology was investigated by transmission electron microscopy (TEM) and nanoscale chemical analysis using electron energy-loss spectroscopy (EELS). Diffraction contrast images (Fig. 1a in plane view and Fig. 1b in cross-section) show self-assembled nanocolumns extending through the whole thickness of the GeMn layer. Mn chemical maps from EELS measurements (Fig. 2) clearly show that the columns are Mn-rich, whereas the signal in the matrix is below the detection limit ( $\sim 1\%$ ). Cross-section images at high resolution (not shown) demonstrate that the epitaxy of the GeMn layer is fully coherent on the Ge buffer layer, and they do not reveal any defect or other phases. Note however that the thickness probed in the cross-section images is much larger than the diameter of the columns, so we mainly observe the structure of the surrounding matrix. We were able to isolate single nanocolumns in high-resolution plane views of the thinnest parts of the sample (Fig. 1c). Around each column, a dark ring reveals a large strain extending over a few interatomic distances. The columns are crystallized, either fully, or in their outermost part, with a clear relationship with the matrix structure. The presence of a disordered core in some columns can reveal a plastic relaxation of the misfit stress with the surrounding matrix; a probable origin, however, is disorder induced by the high-energy electron beam of the microscope (indeed, as will be discussed below, columns are metastable and disappear after annealing at high temperature). A systematic study of high-resolution plane views allowed us to derive the structure of crystallized nanocolumns. They have a diamond structure

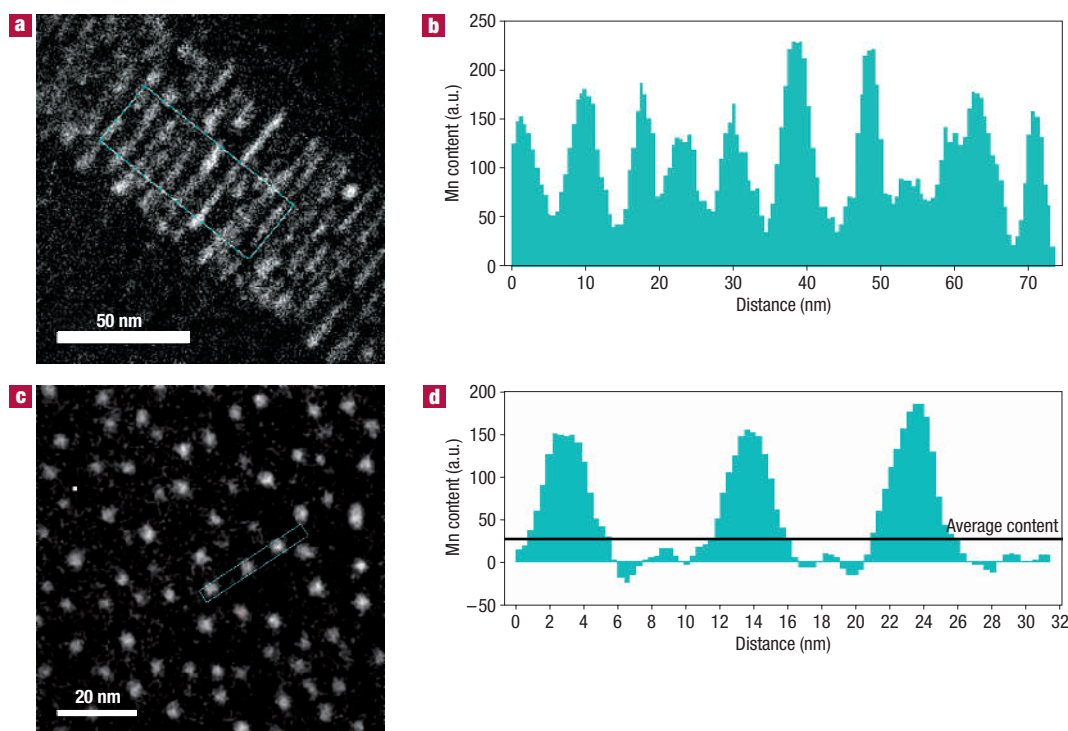


**Figure 2** Mn chemical maps and Mn profiles derived from electron energy-loss spectroscopy. **a,b**, Cross-section, **c,d**, plane view. We recorded 16 pictures in the energy range 500–725 eV every 15 eV on both sides of the Mn  $L_{1,2}$  absorption edge at 650 eV. The energy background was carefully subtracted using the pre-edge pictures. We followed the same procedure for Ge chemical maps. By comparing the Ge signal in the buffer with the GeMn film, we confirm the average Mn concentration of 6%. The relatively high background signal in **b** is due to nanocolumns that superimpose in the cross-section image, whereas the background signal between nanocolumns in **d** gives an estimation of the noise level in these spectroscopic measurements.

elongated along the  $[110]$  or  $[\bar{1}\bar{1}0]$  direction. Nanocolumns are coherently strained in compression by the matrix along one direction ( $[110]$  in Fig. 1d), whereas they are fully relaxed in the perpendicular direction ( $[\bar{1}\bar{1}0]$  in Fig. 1e). Indeed, we observe one additional atomic plane on the matrix side in the relaxed direction with a dislocation at the interface between the matrix and the nanocolumn (see Fig. 1e). In this direction, the nanocolumn lattice exhibits a 4% elongation. Moreover, this elongation is observed either along the  $[110]$  or  $[\bar{1}\bar{1}0]$  direction, in agreement with the cubic symmetry of the matrix.

A Fourier transform of the TEM plane views features a single ring, revealing an isotropic distribution of the columns with a preferential spacing of  $10 \pm 3$  nm; their average diameter is  $3 \pm 0.5$  nm, and the volume fraction is 0.16. Assuming a Mn concentration between 0 and 1% in the matrix leads to a Mn concentration between 37.5% and 32% in the columns: this secondary phase has never been observed before and does not correspond to any known magnetic phase of the binary phase diagram<sup>23</sup>. This type of eutectoid growth of nanocolumns has already been observed in GeCr and SiMn films<sup>20,25</sup>. From a thermodynamical point of view, the gain in chemical free energy by forming a secondary phase from the solid solution is counterbalanced by the interface boundary free-energy loss due to elastic strain (visible in Fig. 1c–e). We are investigating the growth kinetics, but the surface diffusion lengths of the Mn atoms must be long enough even at low growth temperature. On annealing under ultrahigh-vacuum conditions, the nanocolumns remain stable up to 400 °C. However a 15 min annealing at 650 °C activates the volume diffusion of Mn atoms, and the nanocolumns collapse into  $\text{Ge}_3\text{Mn}_5$  nanoparticles which are observed in TEM images at the

bottom of the GeMn layer. Their average diameter derived from XRD data and TEM is 10–12 nm, and EELS confirms a high Mn content in these nanoparticles.

Figure 3a shows the temperature dependence of the magnetization at 2 T, measured by superconducting quantum interference device (SQUID) magnetometry. The magnetic moment per Mn atom is  $4.7 \mu_B$  at 3 K. This value is close to  $5 \mu_B$  expected for isolated  $\text{Mn}^{2+}$  ions according to Hund's rule. The large magnetization at high temperature is consistent with a ferromagnetic phase with  $T_C > 400$  K. ZFC and FC curves superimpose from 3 to 300 K (Fig. 3b), thus ruling out the presence of nanoparticles except if their blocking temperature exceeds 300 K. This is in contrast to the magnetic properties of an annealed layer, characterized by a Curie temperature of  $\sim 300$  K corresponding to the  $\text{Ge}_3\text{Mn}_5$  metallic phase, with ZFC-FC curves (inset in Fig. 3b) exhibiting a blocking temperature of 250 K, in agreement with the observation of nanoparticles in TEM images. Considering the Mn distribution in the GeMn films, we attribute this high- $T_C$  ferromagnetic phase to the nanocolumns. In the low temperature range, the magnetization increases when decreasing the temperature (inset in Fig. 3a). The corresponding saturation magnetization is small ( $\sim 9 \text{ kA m}^{-1}$ ), and the additional susceptibility is described by a Curie–Weiss temperature between 10 and 15 K. A similar behaviour was reported<sup>10</sup> for a strongly diluted  $\text{Ge}_{1-x}\text{Mn}_x$  layer: assuming that Mn atoms are present in the matrix, all magnetically active with a magnetic moment of  $3 \mu_B$  (ref. 26), we determine a Mn concentration of 0.7%, in agreement with the upper limit from EELS (1%). Then, the Mn concentration in the nanocolumns reaches 33.7% (their composition is close to  $\text{Ge}_2\text{Mn}$ ), with a magnetic moment of  $4.9 \mu_B$  per Mn atom as derived from

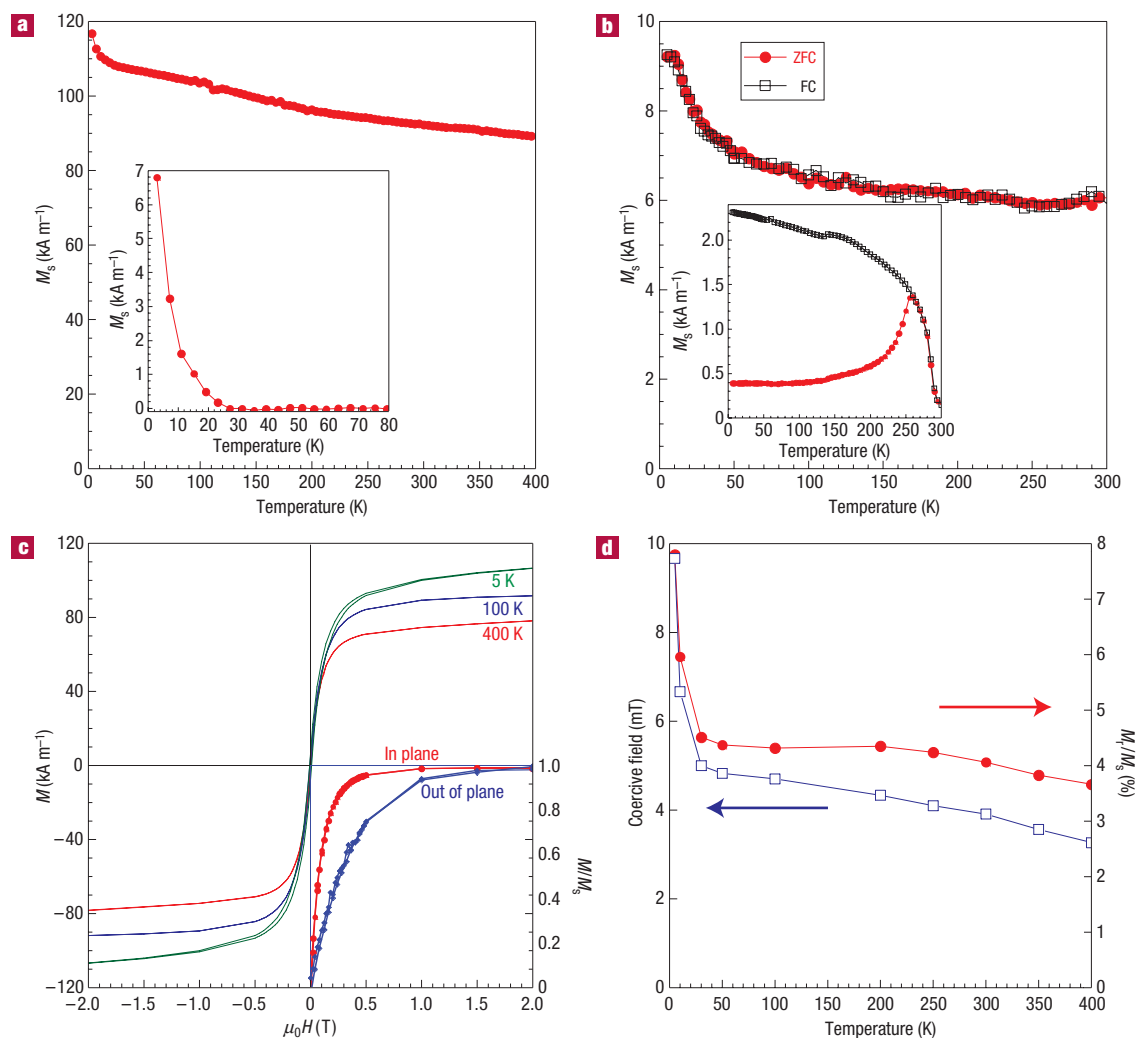


**Figure 3** Magnetic measurements using a SQUID magnetometer. Magnetic fields are applied in the plane along the [100] direction. **a**, Temperature dependence of the saturation magnetization measured at 2 T. The inset shows the extrapolated matrix signal at low temperature after subtracting the nanocolumns magnetic signal. **b**, ZFC-FC measurements carried out at 0.01 T. Both curves superimpose. Inset: ZFC-FC curves after 15-mins annealing at 650 °C. **c**, Magnetization loops at 5, 100 and 400 K, after subtracting the diamagnetic contribution from the substrate. The inset demonstrates the easier saturation in-plane at 250 K. **d**, Coercive field ( $\mu_0 H_c$ ) and remanent magnetization ( $M_r/M_s$ ) versus temperature.  $\mu_0 H_c$  and  $M_r/M_s$  are given with a precision of the order of 10%.

the saturation magnetization ( $\sim 680 \text{ kA m}^{-1}$ ) measured by SQUID. Magnetization loops (Fig. 3c) all have a pronounced S-shape, a low remanent magnetization and a low coercive field (Fig. 3d): in-plane and out-of-plane directions act as hard magnetic axes. The saturation is easier with the field applied in-plane (inset in Fig. 3c).

Nanocolumns are very close to one another and a strong magnetostatic or carrier-mediated coupling is expected. We carried out energy calculations using Fourier formalism<sup>27</sup> for an infinite square lattice of nanocolumns defined by the average experimental parameters (spacing 10 nm, diameter 3 nm and height 80 nm), taking into account the long-range dipolar interaction and dipolar self energy of the nanocolumns. Three configurations have been tested: saturated out-of-plane ( $\uparrow\uparrow$ ), saturated in-plane ( $\rightarrow\rightarrow$ ) and antiparallel out-of-plane with  $M = 0$  ( $\uparrow\downarrow$ ). The results are given in units of  $\mu_0 M_s^2 V/2$ , where  $V$  is the volume of the nanocolumns and  $M_s$  is their magnetization at saturation. The smallest energy,  $E_{\uparrow\downarrow} \approx 0.01$ ,

corresponds to the antiparallel out-of-plane configuration: dipolar interactions favour an antiparallel arrangement of first-neighbour nanocolumns. This finding is in good agreement with the low remanent magnetizations, low coercive fields and S-shaped in-plane and out-of-plane magnetization curves measured by SQUID. Similar magnetic properties have been observed for self-organized cobalt nanopillars grown on a Au(111) surface<sup>28</sup>. In real samples, the remanent magnetization is not zero because nanocolumns are randomly distributed, leading to many frustrated magnetic configurations. The model however fails to predict the right saturated configuration: we calculate  $E_{\rightarrow\rightarrow} \approx 0.46$  and  $E_{\uparrow\uparrow} \approx 0.08$ , whereas experimentally the magnetization is easier to saturate in-plane ( $E_{\rightarrow\rightarrow} < E_{\uparrow\uparrow}$ ). Thus, we must assume that an additional in-plane magnetocrystalline anisotropy, competing with shape anisotropy, favours the in-plane saturated state. This behaviour has previously been observed in arrays of electrodeposited cobalt nanowires<sup>29</sup>. In GeMn nanocolumns, this magnetocrystalline anisotropy may originate from the broken



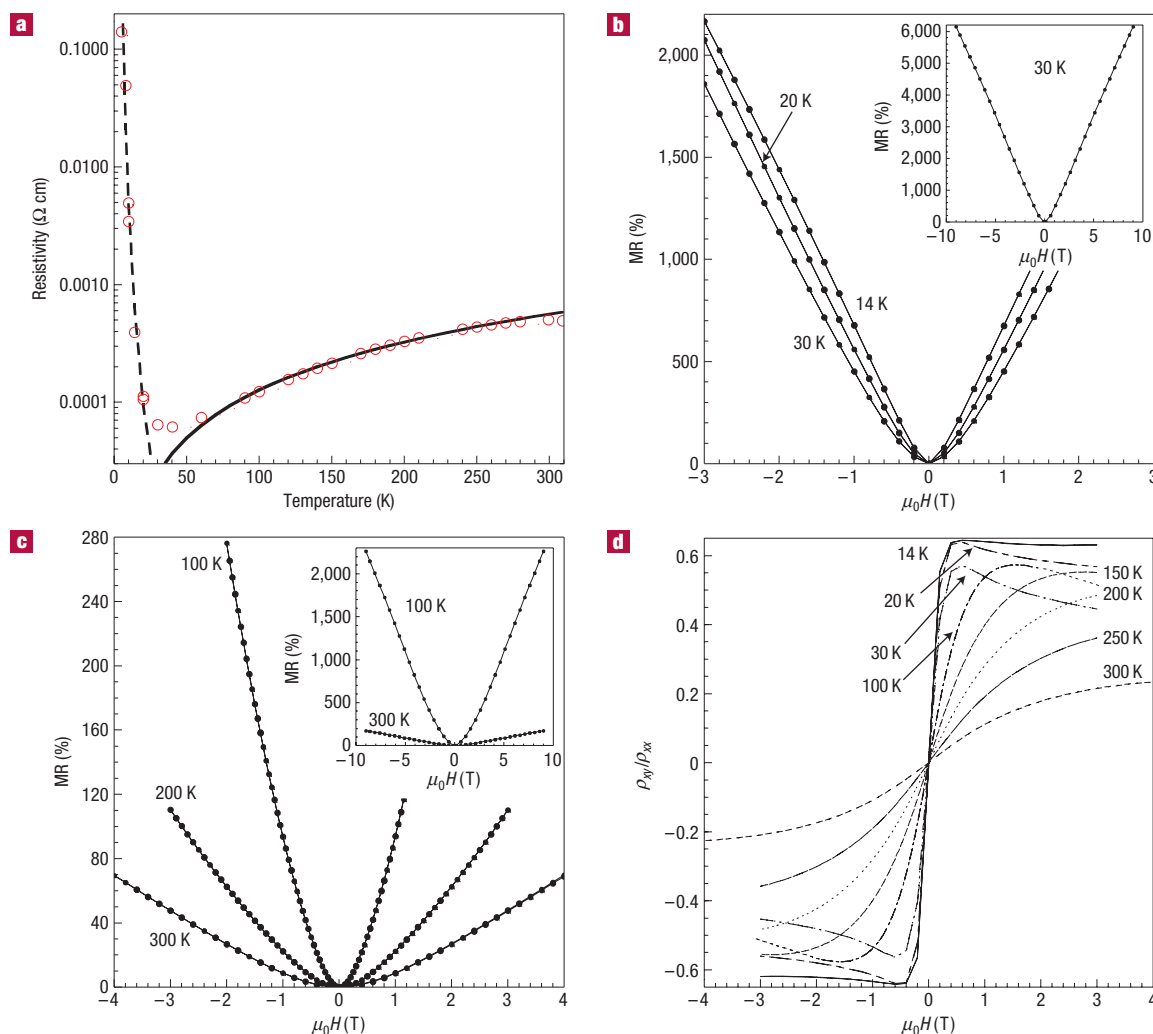


**Figure 4** In-plane magnetotransport measured on 200- $\mu\text{m}$ -wide Hall bars from a  $\text{Ge}_{0.94}\text{Mn}_{0.06}$  film. **a**, Temperature dependence of the zero-field resistivity (open circles). The solid line corresponds to phonon scattering and the dashed line corresponds to variable range hopping. At low temperature (below 6 K), n-type parallel conductivity in the buffer layer limits the resistance divergence and causes an apparent decrease of both the anomalous Hall effect and MR (so that the MR falls to 3% at 6 K and 3 T). **b**, Low-temperature MR with the magnetic field applied perpendicular to the film. Inset: high-field (up to 9 T) MR at 30 K. **c**, High-temperature MR. Inset: high field dependence of the MR at 100 and 300 K. **d**, Hall angle  $\rho_{xy}/\rho_{xx}$  versus magnetic field recorded at different temperatures. The strong AHE loops must be compared with the perpendicular magnetization loops measured by SQUID. Note two effects owing to the strong MR: at low temperature and high field, the magnetization is saturated, so that on the plot of  $\rho_{xy}/\rho_{xx}$ , the normal Hall effect gives rise to an apparent decrease of the Hall angle when divided by the resistivity, whereas on a plot of  $\rho_{xy}$  (not shown) the saturation of the magnetization is washed out by the resistivity increase.

in-plane cubic symmetry (columns are fully strained in only one direction) leading to a natural uniaxial anisotropy combined with large magneto-elastic effects (columns are 4% contracted). As previously discussed in III–V and II–VI ferromagnetic DMSs<sup>30,31</sup>, strain can modify the valence-band dispersion and induce a large magnetic anisotropy. Carrier-mediated ferromagnetic coupling between the nanocolumns would also favour an in-plane saturated state. Finally, in calculating the self energy, we may overestimate the column aspect ratio because the columns are not perfect cylinders.

At this stage, the origin of ferromagnetism inside the columns is unknown: it may be either hole-mediated or itinerant-like. It can also be sensitive to the one-dimensional character of the nanocolumns (see refs 32,33).

The temperature dependence of the zero-field resistivity (Fig. 4a) shows a clear activation at low temperature and a trend

to saturate at high temperature, typical of a doped semiconductor on the insulating side of the metal–insulator transition. Above 30 K, the small decrease with temperature is well fitted by a power law  $T^\alpha$  with  $\alpha \approx 1.4$ , close to the value  $3/2$  predicted for hole scattering by acoustic phonons in germanium<sup>34</sup>. Below 30 K, we observe an exponential dependence on  $T^{-\alpha}$  with  $\alpha \approx 0.3$ , close to the value  $1/4$  typical for variable range hopping<sup>35</sup>. In clean p-doped Ge, such an insulating behaviour is expected below the Mott critical density ( $2 \times 10^{17} \text{ cm}^{-3}$ ); an insulating behaviour at a density larger than the Mott density of the host material is, however, a common observation in disordered systems such as DMSs. The Hall coefficient at 300 K and 9 T is positive (as expected from the acceptor character of Mn in germanium<sup>36</sup>) and the slope is the same as that of an ordinary Hall effect with a carrier density of  $2 \times 10^{19} \text{ cm}^{-3}$ . However, this is a lower bound of the carrier density

because the Hall resistance shows a sub-linear dependence on field, which suggests a contribution from anomalous Hall effect (AHE), as discussed below.

The most dramatic observation is the strong positive MR, as high as 7,000% at 30 K and still 200% at 300 K at 9 T (Fig. 4b,c), which we attribute to a geometrically enhanced orbital MR<sup>37</sup> owing to the presence of the nanocolumns. In this case, the MR intensity will depend on the size and density of the nanocolumns. Such a strong positive MR has never been observed before in dilute GeMn films or in other ferromagnetic semiconductors such as GaMnAs (ref. 38) and ZnMnTe (ref. 8) where a large negative MR is usually observed due to the scattering of carriers by spin disorder. Orbital MR is positive and proportional to  $(\mu_0 H \mu)^2$  (where  $\mu$  is the hole mobility) at low field and saturates at higher field. However, a reasonable value of the low-temperature mobility of holes in germanium with p-doping levels of  $10^{18}$ – $10^{20}$  cm<sup>-3</sup> is  $\sim 10^2$  cm<sup>2</sup> V<sup>-1</sup> s<sup>-1</sup> (ref. 39), therefore orbital MR is too small to account for our MR results. In granular metallic and hybrid systems such as Co/Cu and MnAs/GaAs (refs 40,41), a negative MR is measured, and in any case the present MR is not related to the magnetic properties of the nanocolumns because their magnetization is saturated above 2 T while MR keeps increasing. Possible positive MR effects arise from quantum corrections (electron–electron interaction and weak localization effects) to the Boltzmann conductivity, as discussed by Sawicki *et al.*<sup>42</sup> in CdMnSe and Shapira *et al.*<sup>43</sup> for CdMnTe, or localization of holes on Mn impurities giving rise to an exponential dependence of the resistivity on the magnetic field<sup>35</sup>: we cannot exclude such a contribution below 30 K. Geometrically enhanced orbital MR may give rise to a large positive MR if the nanocolumns (presumably highly p-doped) can be considered as highly conducting inclusions in a semiconducting matrix<sup>37</sup>. The electric field **E** is normal to the surface of a column. In a zero magnetic field, the current density **j** is parallel to **E** so that the low-resistance current path provided by the columns results in an overall sample conductance which is enhanced with respect to that of the homogeneous Ge matrix. At high magnetic fields, that is, for Hall angles close to 90°, **j** is perpendicular to **E** and the current is deflected around the columns. The sample conductance is then reduced compared with that of the homogeneous semiconductor because of the reduction in surface area available. The crossover magnetic field is given by  $\mu_0 H \approx 1/\mu$ . Therefore, at low magnetic fields, the MR follows a  $(\mu_0 H \mu)^2$  law up to the crossover field above which the positive MR rises due to geometrical effects.

We must take into account the strong MR when discussing the Hall effect. If we plot  $\rho_{xy}(H)/\mu_0 M(H)$  versus  $\rho_{xx}(H)$ , where  $\rho_{xy}(H)$  and  $\rho_{xx}(H)$  are the transverse resistivity and the longitudinal resistivity, respectively, and  $\mu_0 M(H)$  is the magnetization derived from perpendicular SQUID measurements, we find (not shown) a clear linear dependence: this shows that the measured Hall effect is dominated by an AHE due to skew scattering<sup>44</sup>. Therefore, to compare AHE and SQUID magnetization, Fig. 4d shows the Hall angle  $\rho_{xy}/\rho_{xx}$  versus the applied magnetic field. The AHE loops are similar to the magnetization loops measured by SQUID with a perpendicular field, at all temperatures, and clearly exhibit the magnetic saturation of the nanocolumns. Moreover, the saturation Hall angle ( $\sim 37^\circ$ ) is much larger than that in other FMS. For instance, Hall angles are five times smaller in II–VI FMS (ref. 8) and one order of magnitude smaller in GaMnAs (ref. 7). This strongly suggests that a large spin polarization of the hole gas is induced by the magnetization of the nanocolumns.

In conclusion, we have shown a new high- $T_C$  ferromagnetic GeMn phase with a composition close to Ge<sub>2</sub>Mn in the form of nanocolumns. This Ge-rich phase is the result of Mn segregation

in the germanium matrix to form nanocolumns during the film growth. Magnetotransport measurements showed a large positive MR related to the particular morphology of the GeMn films, as well as a large AHE due to spin-dependent hole scattering on the ferromagnetic nanocolumns. This result is very promising for future spintronic applications because these ferromagnetic nanocolumns could act as nanochannels for spin injection into silicon or germanium. This inhomogeneous material may also be used as a magnetic-field sensor for its large positive MR, as well as for magnetic recording media if self-organization of the nanocolumns can be achieved.

## METHODS

Growth was carried out by molecular beam epitaxy using standard Ge and Mn effusion cells, at a low deposition rate ( $0.22 \text{ \AA s}^{-1}$ ); the substrate was epi-ready Ge(001) wafers with a residual n-type doping ( $n \approx 10^{15} \text{ cm}^{-3}$ ,  $\rho \approx 5 \text{ \Omega cm}$ ). After thermal desorption of the surface oxide, a 40-nm-thick Ge buffer layer was grown at 250 °C, resulting in a perfect  $2 \times 1$  surface reconstruction as observed by reflection high-energy electron diffraction. 80-nm-thick Ge<sub>1-x</sub>Mn<sub>x</sub> films were subsequently grown, at low temperature (70–130 °C) to minimize phase separation owing to the low solubility of Mn in Ge. The properties described here (magnetic signal at high temperature) have been observed only on samples with quite a high Mn content (6%) grown in a very narrow temperature range around 130 °C. For growth temperatures below 100 °C, nanocolumns exhibit another structure and a very low Curie temperature, whereas for growth temperatures above 200 °C additional spots appear in the reflection high-energy electron diffraction pattern due to the formation of secondary phase crystallites (Ge<sub>3</sub>Mn<sub>5</sub>). By continuously increasing the growth temperature between 100 and 200 °C, we first grow pure high- $T_C$  nanocolumns, and then we obtain a mix of high- $T_C$  nanocolumns with Ge<sub>3</sub>Mn<sub>5</sub> crystallites. A slightly diffuse  $1 \times 1$  streaky pattern is observed throughout the growth indicating predominantly two-dimensional growth. The Mn content is determined using X-ray fluorescence on very thick samples and Rutherford back scattering on (Ge, Mn) films grown on silicon. These two techniques lead to Mn concentrations from 5 to 7%. Consequently, Mn contents as well as magnetic moments are given with an uncertainty of the order of 17%. High-resolution XRD  $\theta/2\theta$  scans carried out on the epitaxial layers show only the germanium (004) diffraction peak in the range:  $15^\circ < 2\theta < 150^\circ$ , in spite of high dynamics of the order of  $10^7$ . Moreover, thickness fringes observed beside the (004) diffraction peak correspond to a 120-nm-thick layer, that is, the total thickness (Ge buffer + Ge<sub>1-x</sub>Mn<sub>x</sub> film). Thus, XRD data revealed no secondary phases in the detection limits of our set up and confirm the high quality of the interface between the Ge buffer and the Ge<sub>1-x</sub>Mn<sub>x</sub> film. In contrast, on the same layers but annealed at 650 °C for 15 min, the (002) and (004) diffraction lines Ge<sub>3</sub>Mn<sub>5</sub> are clearly seen.

Received 1 March 2006; accepted 17 May 2006; published 9 July 2006.

## References

- MacDonald, A. H., Schiffer, P. & Samarth, N. Ferromagnetic semiconductors: moving beyond (Ga,Mn)As. *Nature Mater.* **4**, 195–202 (2005).
- Zutic, I., Fabian, J. & Das Sarma, S. Spintronics: Fundamentals and applications. *Rev. Mod. Phys.* **76**, 323–410 (2004).
- Dietl, T. Ferromagnetic semiconductors. *Semicond. Sci. Technol.* **17**, 377–392 (2002).
- Timm, C. Disorder effects in diluted magnetic semiconductors. *J. Phys. Condens. Matter* **15**, R1865–R1896 (2003).
- Sato, K., Katayama-Yoshida, H. & Dederichs, P. H. High Curie temperature and nano-scale spinodal decomposition phase in dilute magnetic semiconductors. *Jpn J. Appl. Phys.* **44**, L948–L951 (2005).
- Ohno, H., Munekata, H., Penney, T., von Molnar, S. & Chang, L. L. Magnetotransport properties of p-type (In,Mn)As diluted magnetic III–V semiconductors. *Phys. Rev. Lett.* **68**, 2664–2667 (1992).
- Ohno, H. Making nonmagnetic semiconductors ferromagnetic. *Science* **281**, 951–956 (1998).
- Ferrand, D. *et al.* Carrier-induced ferromagnetism in p-Zn<sub>1-x</sub>Mn<sub>x</sub>Te. *Phys. Rev. B* **63**, 085201 (2001).
- Jungwirth, T. *et al.* Prospects for high temperature ferromagnetism in (Ga,Mn)As semiconductors. *Phys. Rev. B* **72**, 165204 (2005).
- Park, Y. D. *et al.* A Group-IV ferromagnetic semiconductor Mn<sub>2</sub>Ge<sub>1-x</sub>. *Science* **295**, 651–654 (2002).
- Li, A. P., Shen, J., Thompson, J. R. & Weitering, H. H. Ferromagnetic percolation in Mn<sub>2</sub>Ge<sub>1-x</sub> dilute magnetic semiconductor. *Appl. Phys. Lett.* **86**, 152507–152509 (2005).
- Cho, S. *et al.* Ferromagnetism in Mn-doped Ge. *Phys. Rev. B* **66**, 033303 (2002).
- Pinto, N. *et al.* Magnetic and electronic transport percolation in epitaxial Ge<sub>1-x</sub>Mn<sub>x</sub> films. *Phys. Rev. B* **72**, 165203 (2005).
- Tsui, F. *et al.* Novel germanium-based magnetic semiconductors. *Phys. Rev. Lett.* **91**, 177203–177206 (2003).
- Braak, H. *et al.* Magnetic characteristics of epitaxial Ge(Mn,Fe) diluted films—a new room temperature magnetic semiconductor? *J. Magn. Magn. Mater.* **286**, 46–50 (2005).
- Kang, J.-S. *et al.* Spatial chemical inhomogeneity and local electronic structure of Mn-doped Ge ferromagnetic semiconductors. *Phys. Rev. Lett.* **94**, 147202 (2005).

17. Sugahara, S., Lee, K. L., Yada, S. & Tanaka, M. Precipitation of amorphous ferromagnetic semiconductor phase in epitaxially grown Mn-doped Ge thin films. *Jpn J. Appl. Phys.* **44**, L1426–L1429 (2005).
18. Dormann, J. L., Fiorani, D. & Tronc, E. *Advances in Chemical Physics* (Wiley, New York, 1997).
19. Goswami, R. *et al.* Growth of ferromagnetic nanoparticles in Ge:Fe thin films. *Appl. Phys. Lett.* **86**, 032509 (2005).
20. Goswami, R., Kioseoglou, G., Hanbicki, A. T., Jonker, B. T. & Spanos, G. Formation of Cr-germanide nanoparticles during growth of epitaxial Ge-Cr thin films. *Acta Mater.* **52**, 2419–2427 (2004).
21. Park, Y. D. *et al.* Magnetoresistance of Mn:Ge ferromagnetic nanoclusters in a diluted magnetic semiconductor matrix. *Appl. Phys. Lett.* **78**, 2739–2741 (2001).
22. D'Orazio, F. *et al.* Magneto-optical study of Mn ions implanted in Ge. *IEEE Trans. Magn.* **38**, 2856 (2002).
23. Massalski, T. B. (ed.) *Binary Alloy Phase Diagrams* 2nd edn, Vol. 2, 1964 (American Society for Metals, Metals Park, Ohio, 1990).
24. Wachtel, E. & Henig, E.-T. Aufbau des systems mangan-germanium. *Z. Metallkd.* **60**, 243–248 (1969).
25. Zhang, Y., Jiang, Q., Smith, D. J. & Drucker, J. Growth and characterization of  $\text{Si}_{1-x}\text{Mn}_x$  alloys on  $\text{Si}(100)$ . *J. Appl. Phys.* **98**, 033512 (2005).
26. Schulthess, T. C. & Butler, W. H. Electronic structure and magnetic interactions in Mn doped semiconductors. *J. Appl. Phys.* **89**, 7021–7023 (2001).
27. Beleggia, M., Tandon, S., Zhu, Y. & De Graef, M. On the magnetostatic interactions between nanoparticles of arbitrary shape. *J. Magn. Magn. Mater.* **278**, 270–284 (2004).
28. Fruchart, O., Klaua, M., Bartel, J. & Kirschner, J. Self-organized growth of nanosized vertical magnetic Co pillars on  $\text{Au}(111)$ . *Phys. Rev. Lett.* **83**, 2769–2772 (1999).
29. Darques, M., Encinas, A., Vila, L. & Piroux, L. Tailoring of the c-axis orientation and magnetic anisotropy in electrodeposited Co nanowires. *J. Phys. C* **16**, S2279–S2286 (2004).
30. Dietl, T., Ohno, H. & Matsukura, F. Hole-mediated ferromagnetism in tetrahedrally coordinated semiconductors. *Phys. Rev. B* **63**, 195205 (2001).
31. Kossacki, P. *et al.* Spin engineering of carrier-induced magnetic ordering in  $(\text{Cd,Mn})\text{Te}$  quantum wells. *Physica E* **21**, 943–946 (2004).
32. Song, Y. P. *et al.* Physical origin of the ferromagnetic ordering above room temperature in  $\text{GaMnN}$  nanowires. *J. Phys. C* **17**, 5073–5085 (2005).
33. Kazakova, O., Kulkarni, J. S., Holmes, J. D. & Demokritov, S. O. Room temperature ferromagnetism in  $\text{Ge}_{1-x}\text{Mn}_x$  nanowires. *Phys. Rev. B* **72**, 094415 (2005).
34. Sze, S. M. *Physics of Semiconductors Devices* (Wiley, New York, 1981).
35. Schklovskii, B. I. & Efros, A. L. *Electronic Properties of Doped Semiconductors* (Springer, Berlin, 1984).
36. Woodbury, H. H. & Tyler, W. W. Properties of germanium doped with manganese. *Phys. Rev.* **100**, 659–662 (1955).
37. Solin, S. A., Thio, T., Hines, D. R. & Heremans, J. J. Enhanced room-temperature geometric magnetoresistance in inhomogeneous narrow-gap semiconductors. *Science* **289**, 1530–1532 (2000).
38. Van Esch, A. *et al.* Interplay between the magnetic and transport properties in the III-V diluted magnetic semiconductor  $\text{Ga}_{1-x}\text{Mn}_x\text{As}$ . *Phys. Rev. B* **56**, 13103–13112 (1997).
39. Golikova, O. A., Moizhes, B. Y. & Stilbans, L. S. Hole mobility of germanium as a function of concentration and temperature. *Sov. Phys. Solid State* **3**, 2259–2265 (1962).
40. Berkowitz, A. E. *et al.* Giant magnetoresistance in heterogeneous Cu-Co alloys. *Phys. Rev. Lett.* **68**, 3745–3748 (1992).
41. Akinaga, H. *et al.* Negative magnetoresistance in GaAs with magnetic MnAs nanoclusters. *Appl. Phys. Lett.* **72**, 3368–3370 (1998).
42. Sawicki, M. *et al.* Influence of s-d exchange interaction on the conductivity of  $\text{Cd}_{1-x}\text{Mn}_x\text{Se:In}$  in the weakly localized regime. *Phys. Rev. Lett.* **56**, 508–511 (1986).
43. Shapira, Y., Oliveira, N. F., Becla, P. & Vu, T. Q. Magnetoresistance and Hall effect near the metal-insulator transition of n-type  $\text{Cd}_{0.95}\text{Mn}_{0.05}\text{Te}$ . *Phys. Rev. B* **41**, 5931–5941 (1990).
44. Chazalviel, J.-N. Spin-dependent Hall effect in semiconductors. *Phys. Rev. B* **11**, 3918–3934 (1975).

Correspondence and requests for materials should be addressed to M.J.  
Supplementary Information accompanies this paper on [www.nature.com/naturematerials](http://www.nature.com/naturematerials).

### Competing financial interests

The authors declare that they have no competing financial interests.

Reprints and permission information is available online at <http://npg.nature.com/reprintsandpermissions/>